Insights into transition metal encapsulated N-doped CNTs cathode for self-sufficient electrocatalytic degradation

Pei Su [a,b,c], Wenyang Fu [a,b,c], Zhongzheng Hu [a,b,c], Jiana Jing [a,b,c], Minghua Zhou [a,b,c,*]

[a] Key Laboratory of Pollution Process and Environmental Criteria, Ministry of Education, College of Environmental Science and Engineering, Nankai University, Tianjin 300350, China
[b] Tianjin Key Laboratory of Environmental Technology for Complex Trans-Media Pollution, College of Environmental Science and Engineering, Nankai University, Tianjin 300350, China
[c] Tianjin Advanced Water Treatment Technology International Joint Research Center, College of Environmental Science and Engineering, Nankai University, Tianjin 300350, China

ARTICLE INFO

ABSTRACT

In electrochemical advanced oxidation processes (EAOPs), a series of transition metal encapsulated nitrogen-doped carbon nanotubes (M@N-C, M=Fe, Co, Ni, Cu) as bifunctional cathodes were synthesized to compare and uncover their activity trends, fulfilling the self-sufficient electrocatalytic degradation. The sulfamethazine (SMT) degradation activity trends were follows: Co@N-C>Fe@N-C>Ni@N-C>Cu@N-C cathode at pH$\leq$ 7, while the Fe@N-C cathode exhibited the highest activity at pH 9 due to the more $^1O_2$ and atomic H*. In-situ Fourier transformed infrared (FTIR) spectroscopy and density functional theory (DFT) calculation suggested that the atomic H* was easier to generate under the action of pyridinic N on Fe@N-C cathode. Overall, various pollutants degradation on Fe@N-C cathode performed with good stability with low leaching iron (0.12 mg L^{-1}) and low energy consumption ($<$0.3 kWh$\cdot$log$^{-1}\cdot$m^{-3}). This study sheds light on different mechanisms of reactive species production on M@N-C cathode, thus providing guidance for the selectivity between M@N-C via active species and pollutants.

1. Introduction

Electrochemical advanced oxidation process (EAOPs), which can produce highly oxidative hydroxyl radicals ($^\bullet$OH), have been a promising approach for mineralization of refractory organic pollutants from wastewater [1,2]. Among these EAOPs, the Fe^{2+}-initiated electro-Fenton (EF) produces $^\bullet$OH via reaction with homogeneous Fe^{2+} catalyst and electrochemically generated H_2O_2, which avoids the risks in transportation, storage and usage of H_2O_2 [3–5]. However, the inherent limitation to conventional homogenous EF is that catalytic performance is highly pH-dependent, poor stability and large iron sludge production [6–8]. To overcome this limitation and exert catalytic performance, it is generally acknowledged that heterogeneous EF using bifunctional cathode to facilitate the 2e$^-$ oxygen reduction reaction (ORR) and reactive species formation is potential alternative [9,10], thus it is very important to design novel bifunctional cathode to fulfill self-sufficient electrocatalytic degradation [11].

Introduction of heteroatom such as nitrogen, sulfur and phosphorous into carbon framework could change the chemical properties of carbon materials to improve catalytic activity [12,13]. It was reported that the introduction of N into graphene was conductive to H_2O_2 generation due to the introduction of graphite N, while the introduced pyridinic N promoted the decomposition of H_2O_2 to $^\bullet$OH [14,15]. Because this process required two-stages electron transfer (2e$^-$ + e$^-$ process) [12,16], these two stages were competitive and difficult to balance. On the other hand, despite abundant transition metal-based catalysts had been exploited to promote EF efficiency by the yield of $^\bullet$OH via Fenton-like catalysis, obvious drawbacks such as fast release of metal ions, slow catalytic kinetics at neutral and alkaline environments were still noticed [17,18]. Later, some Fe-based catalysts were attempted as bifunctional cathode, unfortunately still facing the above shortcomings [8,10,19,20]. In contrast, less attention has been paid to prepare metal-N-C bifunctional cathode with different transition metal centers, let alone disclose the nature of the transition metal on the EF catalytic activities and

---

mechanism towards different reactive species production.

Most of transition metal-C catalysts usually suffer from poor catalytic activity and stability due to the low exposure and utilization of active sites, and poor resistance to acidic corrosion [21,22]. At the same time, metal-N-C catalysts are mainly occurred 4e$^-$ process to produce H_2O [23], which is inapplicable as cathode to generate H_2O_2 in-situ. To overcome such limitations, one promising strategy would be synthesis catalyst with spatial confinement to restrict the distance between metal surface and reactants, decrease the contact between metal and electrolyte, and avoid the loss of short-lived reactive species. The carbon nanotubes (CNTs) have gained considerable attention because of their unique electronic and hollow porous structure properties [24,25]. The pollutants degradation performance was found closely correlated to the efficacy of the Fe_2O_3 confined in CNTs with singlet oxygen ($^1O_2$)-mediated Fenton process, which exhibited wide pH tolerance and high selectivity [18]. EAOPs based on other reactive species apart from $^\bullet OH$ have been the research trend for in-situ removal of pollutants. Therefore, it is imperative to synthesize transition metal-N-C catalysts with uniform structures and metal sites to comprehensively uncover their catalytic activity, and explore reaction mechanism in formation of reactive species, which are essential for pollutant removal to achieve high efficiency and low energy consumption at wide pH ranges.

Sulfamethazine (SMT) is a typical sulfonamide antibiotic (the concentration in wastewater was ranged from 20 to 1000 ng L^{-1}) [26], which has antibacterial activity and is widely used in human and veterinary medicine [27]. However, because of its antibacterial nature and poor biodegradability, SMT cannot be completely remove by conventional wastewater treatment processes [28]. Herein, a series of N-doped CNTs encapsulated transition metal (named as M@N-C, M = Fe, Co, Ni, Cu) were synthesized, which contained different metal species but have similar structural and physicochemical properties to compare and uncover their activities trends and reactive species in self-sufficient electrocatalytic process for SMT degradation. The $^\bullet OH$, $^1O_2$ and atomic H* was detected as the main reactive species using M@N-C cathode for pollutants degradation. Furthermore, density functional theory (DFT) calculations and in-situ Fourier transformed infrared (FTIR) spectroscopy proved that the production of active species was carbon sites near nitrogen, which could trigger generation of atomic H*. The generated trends of various reactive species on M@N-C cathode at different pH were explored, and the mechanism of reactive interaction was disclosed. The application prospect of M@N-C cathode was further examined for treatment of various pollutants and real wastewaters.

2. Experimental section

2.1. Multifunctional cathode preparation

The M@N-C catalysts were prepared based on the carbonization method of melamine, α-cyclodextrin (α-CD) and $Fe(NO_3)_3 \cdot 9\,H_2O$, and the schematic diagram of the preparation of multifunctional cathodes was shown in Fig. S1. In a typical synthesis, melamine (2 g), α-CD (0.4 g) and $Fe(NO_3)_3 \cdot 9\,H_2O$ (0.4 g) was dissolved in the mixture of deionized water (80 mL) and methanol (20 mL). After the above solution was continuously stirred at 80 °C, the precipitates were finely ground to obtain the powder. Next, the powder was annealed at 550 °C for 3 h and further heated at the rate of 5 °C min^{-1} to 900 °C, which remained in Ar atmosphere for 6 h. The as-obtained catalysts were denoted as Fe@N-C (Fe encapsulated in N-doped CNTs). For other M@N-C (M=Co, Ni, Cu) preparation, the $Fe(NO_3)_3 \cdot 9\,H_2O$ was replaced by $Co(NO_3)_2 \cdot 6\,H_2O$, Ni $(NO_3)_2 \cdot 6\,H_2O$ and $Cu(NO_3)_2 \cdot 3\,H_2O$, respectively. The same method as above was carried out but without metal salt to obtain N-C.

For cathode preparation, the obtained N-C and M@N-C was mixed with ethanol (0.5 mL), Nafion solution (5 wt%, 0.05 mL), which was ultrasonically dispersed for 10 min to make the catalyst evenly distributed. Finally, the obtained ink was coated using brush on the carbon cloth (CC) with 3 mg cm^{-2} catalyst loading.

2.2. Electrochemical analysis

5 mg N-C or M@N-C catalysts were dispersed in solution of 600 μL of water, 300 μL of ethanol and 100 μL of Nafion solution under ultrasonication for 30 min. The 10 μL of catalytic ink was loaded on the glassy carbon electrode (GC, area was 0.197 cm^2) as working electrode. The counter electrode was Pt sheet (1 cm × 1 cm) and the reference electrode was Ag/AgCl (saturated KCl) electrode, which could be converted into the reversible hydrogen electrode (RHE) (E (vs. RHE) = E (vs. Ag/AgCl) + 0.224 V + 0.0591 ×pH). The rotating ring disk electrode (RRDE) (Pine Instruments, USA) measurement was carried out to obtain the linear sweep voltammetry (LSV) at the scanning rate of 10 mV s^{-1} and the ring potential of 1.0 V (vs RHE) in the electrolyte of O_2-saturated $HClO_4$ (0.1 M, pH 1), Na_2SO_4 (0.05 M, pH 7) or KOH (0.1 M, pH 13). The ring disk electrode (RDE) measurement was carried out to obtain the cyclic voltammetry (CV) at the scanning rate of 100 mV s^{-1}.

2.3. Characterizations

The morphology of the as-prepared N-C and M@N-C catalysts were investigated by the field-emission scanning electron microscopy (FESEM, LEO-1530VP), transmission electron microscopy (TEM, JEM-2800) and high-resolution TEM (HRTEM, JEM-2100 f). The chemical composition and phase structure of M@N-C was characterized by the X-ray photoelectron spectroscopy (XPS, Thermo Scientifc ESCALAB 250Xi), Raman spectra (ThermoFisher DXR) and X-ray diffraction (XRD, Philips-12045 B/3 diffractometer). The specific surface area and pore distribution were measured by Micromeritics ASAP 2460 instrument though Brunauer-Emmett-Teller (BET) method. Electron paramagnetic resonance (EPR) analysis was carried out using a Bruker EMX Nano (Germany) by employing the reagent 5,5-dimethyl-1-pyrroline N-oxide (DMPO) and 2,2,6,6-Tetramethylpiperidine (TEMP). The concentration of organic pollutants was determined by high-performance liquid chromatograph (HPLC, Ultimate 3000, ThermoFisher, America) equipped with C18 column (3 μm, φ3.0 ×100 mm). The mobile phase and detector wavelength for pollutants detection were shown in Table S1. The metal leaching concentration was quantified by inductively coupled plasma optical emission spectrometer (ICP-OES, Thermo Elemental IRIS Intrepid II XSP). Total organic carbon (TOC) was measured by TOC analyzer (Shimadzu, Japan).

2.4. In-situ Fourier transformed infrared spectroscopy

In-situ FITR was conducted in an external reflection configuration using Thermo Scientific Nicolet IS50 FTIR (Thermo Fisher, USA) and the Ge crystal was used as prism. In three-electrode cell, the working electrode, counter electrode and reference electrode were GC with electrocatalysts ink, Pt wire and Ag/AgCl, respectively. The ink was prepared by 10 mg catalysts, 750 μL ethanol, 200 μL water and 50 μL Nafion solution, and ink of 10 μL was loaded on the GC. The electrolyte was O_2-saturated Na_2SO_4 with SMT of 10 mg L^{-1} at pH = 7. The base spectrum was obtained at − 0.65 V (vs RHE) while the samples spectrum was collected at each 0.1 V potential step between 0.65 V to − 0.35 V (vs RHE), and every piece of FTIR spectrum was captured by consuming 200 s.

2.5. Experimental setup

All organic pollutants degradation experiments were carried out in a three-electrode cell (50 mL, 50 mM Na_2SO_4). The M@N-C loaded CC acted as the working electrode, and dimensionally stable anode (DSA) and saturated calomel electrode (SCE) were used as the counter and reference electrodes, respectively. The potential could be converted to the RHE (E (vs. RHE) = E (vs. SCE) + 0.24 V + 0.0591 ×pH). The scavenger quenching experiments were conducted by adding different scavenger, such as tert-Butanol (TBA, 50 mM) for atomic H* and $^\bullet OH$

[29], methanol (MeOH, 6 M) for •OH [29], benzoquinone (BQ, 50 mM) for $O_2^{•-}$ and furfuryl alcohol (FFA, 50 mM) for $^1O_2$ [9], respectively.

2.6. DFT calculations

Viennea Ab-initio Simulation Package (VASP 5.4.4) was used in DFT calculations. The interaction between ion and electron with cutoff energy of 400 eV was analyzed by the projector augment wave method. The generalized gradient approximation with Perdew-Burke-Ernzerhof (PBE) functional were employed to describe the exchange-correlation term. A $1 \times 1 \times 1$ gamma pack k-point were sampled for geometry optimization. All calculation converged until the forces were below 0.03 eV $Å^{-1}$. The structure of M@N-C based on the literature was that M_4 cluster encapsulated in N-doped single-wall CNTs [30].

3. Results and discussion

3.1. Characterization of M@N-C catalysts

The prepared N-C catalysts exhibited folded laminar structure (Fig. S2), while M@N-C in the FESEM and HRTEM images demonstrated a CNTs structure (Fig. 1a-b and Fig. S2-S4). The zero-valent transition metal (lattice spacing of Fe^0, Co^0, Ni^0 and Cu^0 was 0.20, 0.21, 0.21 and 0.21 nm [31–34], respectively) was encapsulated into CNTs cavity, and the lattice spacing of 0.34 nm was attributed to the graphite carbon (002) in all M@N-C (Fig. 1c-d, Fig. S3-S5). To further confirm the structure of the prepared M@N-C, the drift-corrected EDX line profile corresponding to C-K, O-K, N-K and Fe-K energies was shown in Fig. 1e, the decreasing in the peaks for C and N and the corresponding increase in Fe clearly showed that the core was made of Fe and the shell was made of N-C. The composition of the Fe@N-C structure was performed using elemental mapping for C, N, O and Fe, which also proved the structure of N-C encapsulated Fe (Fig. 1f). The structure of other M@N-C (M = Co, Ni, Cu) was similar with that of Fe@N-C (Fig. S3-S5). The specific surface area of the prepared N-C was about 582 m^2 g^{-1}, however, the surface area of all M@N-C decreased to around 180 m^2 g^{-1} (Fig. S6 and Table S2). The similarity of M@N-C catalysts was evaluated by the Raman spectroscopy and XRD. The intensity ratio of D band to G band (I_D/I_G) [35] for N-C and M@N-C was similar, indicating that the similar structure of M@N-C was exhibited (Fig. 2a). As shown in Fig. 2b, the broad diffraction peaks at 26.1° (002) [36] indexed to the defective structure of graphite carbon in N-C and all M@N-C. For M@N-C catalysts, the peaks in XRD pattern were both indexed to zero-valent Fe, Co,

Ni and Cu, respectively [31,37–39]. These results further identified the similarity on the materials structure and physicochemical properties for M@N-C.

The detailed atomic structure and quantitative elemental analysis of M@N-C were measured by XPS in Fig. S7 and Table S3. All M@N-C exhibited similar metal contents in Fig. 2c (around 1.21–1.37 at%, or around 5.53–6.70 wt%). As shown in Fig. S8, the N1s XPS spectra of N-C could be fitted with pyridinic N/M-N, pyrrolic N, graphite N and oxidized N [14]. The M@N-C exhibited similar N species, and the content of pyridinic N/M-N was higher after introduction of metal (Table S4). The peak of pyridinic N/M-N in M@N-C was not shifted when compared with pyridinic N in N-C, indicating the coordination between metal and pyridinic N was weak. Besides, the zero-valent Fe, Co, Ni and Cu in XPS spectra (Fig. S9) was observed, exhibiting similar zero-valent metal contents (from 13.66 at% to 16.57 at%) [31–34]. In O1s XPS spectra, the zero-valent metal/metal oxide existed after introducing metal, and the -COOH group slightly shifted in M@N-C compared with N-C, indicating that the introduction of metal affected the electron transfer of N-C (Fig. S10) [40]. Overall, it suggested the structural similarity of all M@N-C.

3.2. The H_2O_2 generation on M@N-C

The electrochemical performance of M@N-C for ORR was evaluated by the RRDE method in three O_2-saturated electrolytes including 0.1 M $HClO_4$ (pH = 1), 0.05 M Na_2SO_4 (pH 7) and 0.1 M KOH (pH = 13). Compared with N-C, M@N-C catalysts exhibited high disk current and more positive onset potentials in all pH electrolyte (Fig. 3a-c), indicating that encapsulated metal in M@N-C was both active sites for ORR. The onset potentials of Fe@N-C and Co@N-C was both about 0.744 V (vs RHE), 0.601 V (vs RHE) and 0.748 V (vs RHE) at pH = 1, 7 and 13, respectively. At pH = 1, the highest activity of Co@N-C for ORR was observed, however, it exhibited the strongest hydrogen evolution reaction compared with other M@N-C (Fig. 3a). The overall turn for onset potentials was Co@N-C > Fe@N-C > Ni@N-C > Cu@N-C.

The H_2O_2 selectivity based on the current of ring and disk was calculated to evaluate the H_2O_2 generation, proving the overall selectivity trend was N-C > Fe@N-C > Co@N-C > Ni@N-C > Cu@N-C at pH = 1 and Co@N-C > Fe@N-C > N-C > Ni@N-C > Cu@N-C at pH = 7 and pH = 13, respectively (Fig. 3d). The H_2O_2 selectivity of Fe@N-C and Co@N-C at pH = 7 reached 90% and 91%, respectively. Similar results were observed in alkaline electrolytes, their H_2O_2 selectivity was 93% and 94%, respectively. However, the H_2O_2 selectivity of Co@N-C at
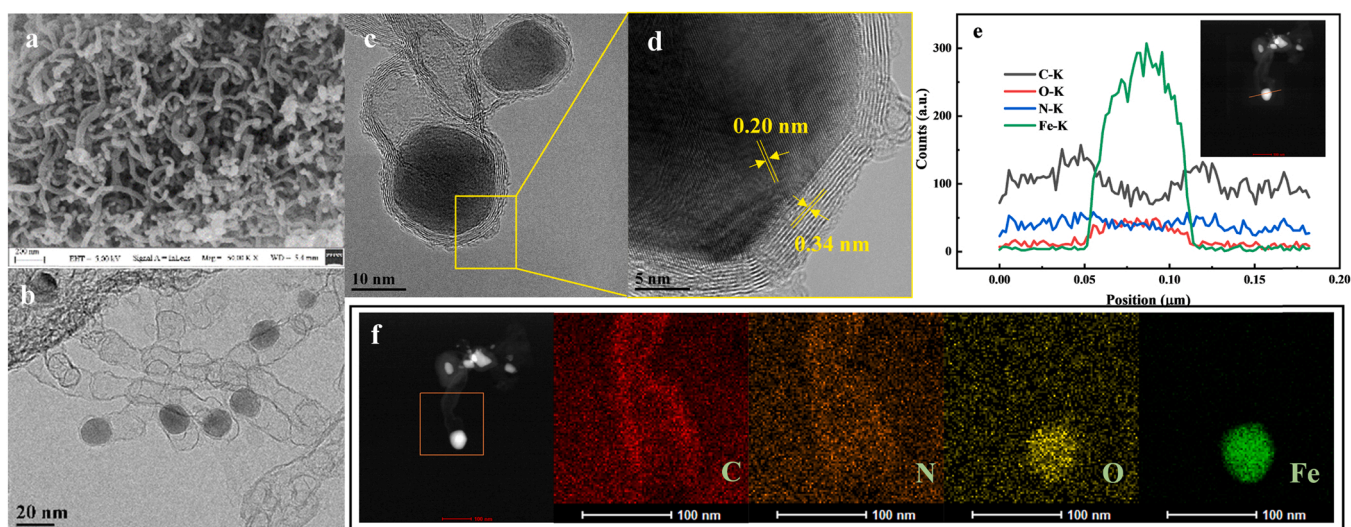

Fig. 1. The (a) FESEM image of Fe@N-C, (b, c and d) the HRTEM image of Fe@N-C, (e) line profile of Fe@N-C, (f) elemental mapping of Fe@N-C (Fe@N-C was taken as the representative example in M@N-C).
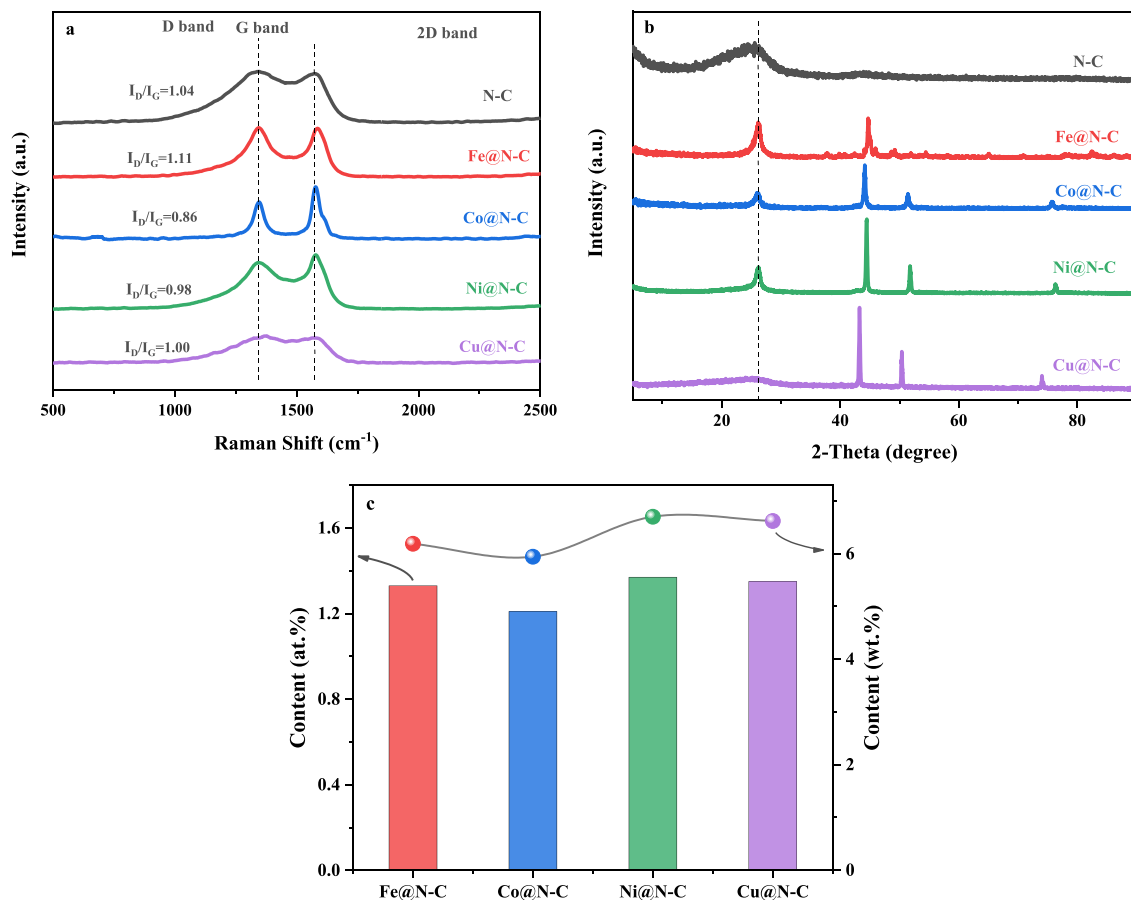
Fig. 2. (a) Raman spectra; (b) XRD pattern of N-C and M@N-C and (c) metal contents ((at% or wt%) of M@N-C obtained by XPS.
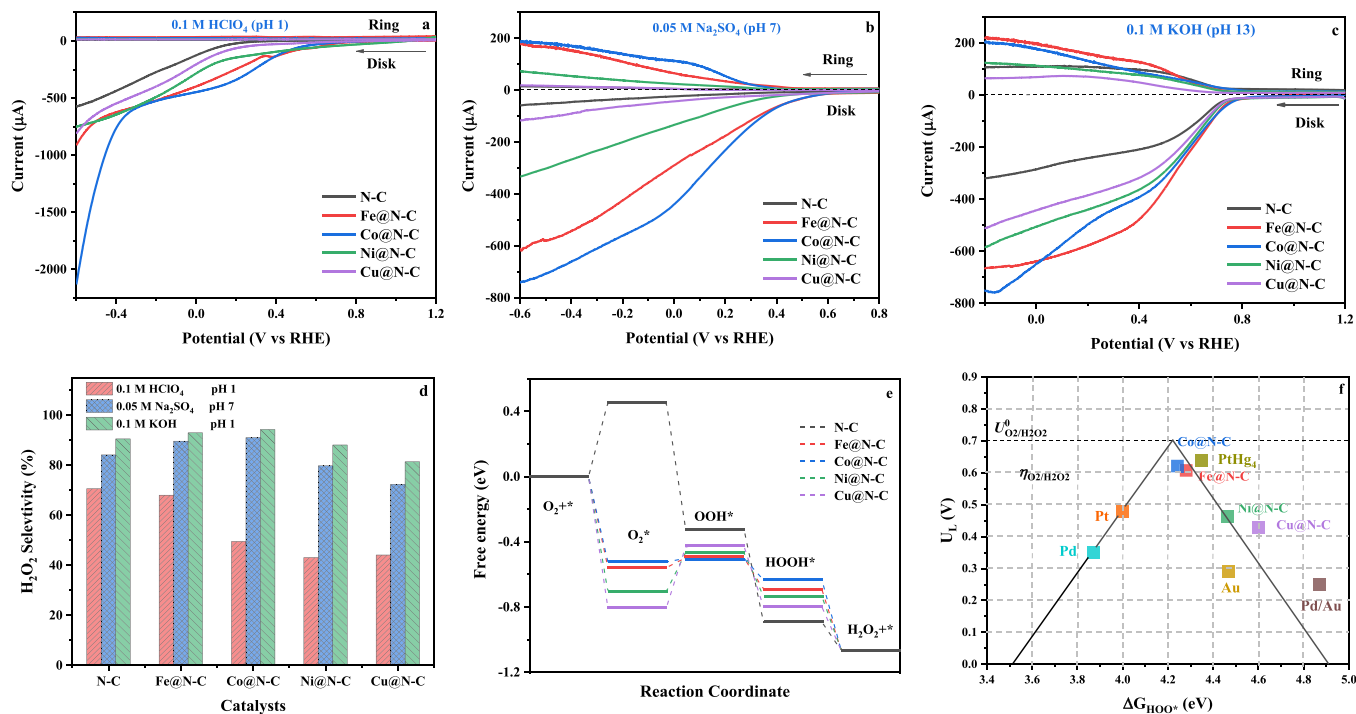

Fig. 3. The LSV curve of M@N-C and N-C at 900 rpm in O_2-saturated (a) 0.1 M $HClO_4$ (pH = 1), (b) 0.05 M Na_2SO_4 (pH = 7) and (c) 0.1 M KOH (pH = 13); (d) the H_2O_2 selectivity of M@N-C and N-C at − 0.15 V (vs RHE) in different electrolytes; (e) the thermodynamic activity of O_2 reduction in 2e- ORR over N-C and M@N-C; (f) calculated Sabatier volcano plot for the 2e$^-$ ORR to H_2O_2 for M@N-C obtained from DFT simulations, the U_L is plotted as a function of ΔG_{*OOH}. The black solid lines represent the theoretical Sabatier volcano.

pH= 1 was only 50% compared with N-C (71%) and Fe@N-C (68%). It was found that the content of graphite N in M@N-C was decisive for H_2O_2 generation at neutral and alkaline environment (Fig. S11a), which was consistent with our previous studies [14]. However, the M@N-C toward H_2O_2 generation was determined by content of -COOH group in the acidic electrolyte (Fig. S11b) [33,41].

In order to further evaluate the ability of M@N-C toward H_2O_2 generation, the DFT calculation was implemented with optimized geometry structures of M@N-C (Fig. S12). The form of free energy diagram of $2e^-$ ORR of M@N-C was shown in Fig. 2e. It could be observed that the adsorption of O_2 (adsorption energy (ΔG_{O_2*}) = 0.46 eV) on N-C was the rate-limiting step toward H_2O_2 generation. The ΔG_{O_2*} was -0.52 eV - -0.81 eV for all M@N-C, and the presence of Co was more conductive for adsorption of O_2 ($\Delta G_{O_2*} = -0.52$ eV). The formation of *OOH as intermediate was supposed to be the rate-limiting step for H_2O_2 generation on M@N-C (Fig. 3e), and the overall turn for ORR activity was Co@N-C > Fe@N-C > Ni@N-C > Cu@N-C, which was consistent with H_2O_2 selectivity. The ORR volcano plot for the $2e^-$ pathway for M@N-C was performed based on the rate-limiting step of *OOH adsorption (ΔG_{*OOH}) (Fig. 3f). The M@N-C toward H_2O_2 generation was influenced by hydrogenation of O_2 because all M@N-C was located in the right-hand side of volcano [42]. The ΔG_{*OOH} of ideal catalysts was 4.22 eV [43]. As shown in volcano, the overall ΔG_{*OOH} trend was Co@N-C (4.24 eV) < Fe@N-C (4.28 eV) < Ni@N-C (4.46 V) < Cu@N-C (4.59 V). Above theoretical calculation results indicated that Co@N-C exhibited superior activity for $2e^-$ ORR, followed by Fe@N-C, which was consistent with metal-nitrogen-carbon (M-N-C) single-atom catalysts for H_2O_2 generation in literature [44].

3.3. Application of M@N-C cathode for organics degradation

The electron transfer ability of M@N-C cathode was investigated to evaluate the catalytic performance. The charge transfer resistance (R_{ct}) of N-C was 120.7 Ω, and R_{ct} was 93.6 Ω for Fe@N-C, 88.3 Ω for Co@N-C, 98.4 Ω for Ni@N-C and 113.4 Ω for Cu@N-C, respectively, indicating that the electron transfer was accelerated after metal introduction and the presence of Co was the most conductive and Fe was the second (Fig. S13) [44]. The SMT degradation was used to evaluate the catalytic activity of M@N-C in electrocatalytic process. As shown in Fig. 4a-c, all M@N-C exhibited a faster SMT degradation compared with N-C with the lower remaining H_2O_2 concentration (Fig. S14a). The SMT degradation followed the sequence of Co@N-C > Fe@N-C > Ni@N-C > Cu@N-C at pH = 3 and 7. As shown in Fig. S14b, the SMT degradation decreased with the increase of pH. However, the Fe@N-C exhibited amazing SMT removal compared with other M@N-C at pH = 9, and the first-order rate constants (k value) of Fe@N-C (0.017 min^{-1}) was 1.73-folds of other M@N-C (0.0095 min^{-1}). Furthermore, the catalytic degradation kinetics of the M@N-C cathode based on the normalizing k value and molar ratio of metal contents was compared in Fig. 4d, the normalized k value of Co@N-C and Fe@N-C was 1.97×10^3 min^{-1} mol^{-1} per mole Co atom sites and 1.57×10^3 min^{-1} mol^{-1} per mole Fe atom sites at pH = 3, and 1.21×10^3 min^{-1} mol^{-1} per mole Co atom sites and 0.90×10^3 min^{-1} mol^{-1} per mole Fe atom sites at pH = 7, and 0.47×10^3 min^{-1} mol^{-1} per mole Co atom sites and 0.75×10^3 min^{-1} mol^{-1} per mole Fe atom sites at pH = 9, respectively. The electrical energy consumption (EEC) per order for 10 mg L^{-1} of SMT removal at pH = 7 was 0.30 and 0.51 kWh·$\log^{-1}$·m^{-3} for Fe@N-C and Co@N-C at low applied current (< 15 mA) and cathode potential (-0.15 V vs RHE), respectively (Fig. S15), which was lower than the reported results in literatures (Table S5). Besides, the degradation efficiency in this work was compared with literatures (Fig. 4e). Fe@N-C and Co@N-C cathode in this work exhibited the degradation rate 2–30 folds of that in literatures. These results supported that the SMT degradation by Fe@N-C and Co@N-C cathode possessed very high normalizing k value and low applied current among different cathodes including FeOx/NHPC [10], FeSCA [45], $Fe^{II}Fe^{III}$ LDH [12] and Fe@Fe_2O_3/ACF [46], and powder heterogeneous catalysts including FeCu@PC [38], Fe/Fe_3C@PC [32] and pyrite [47]. Above results emphasized that the high metal active site
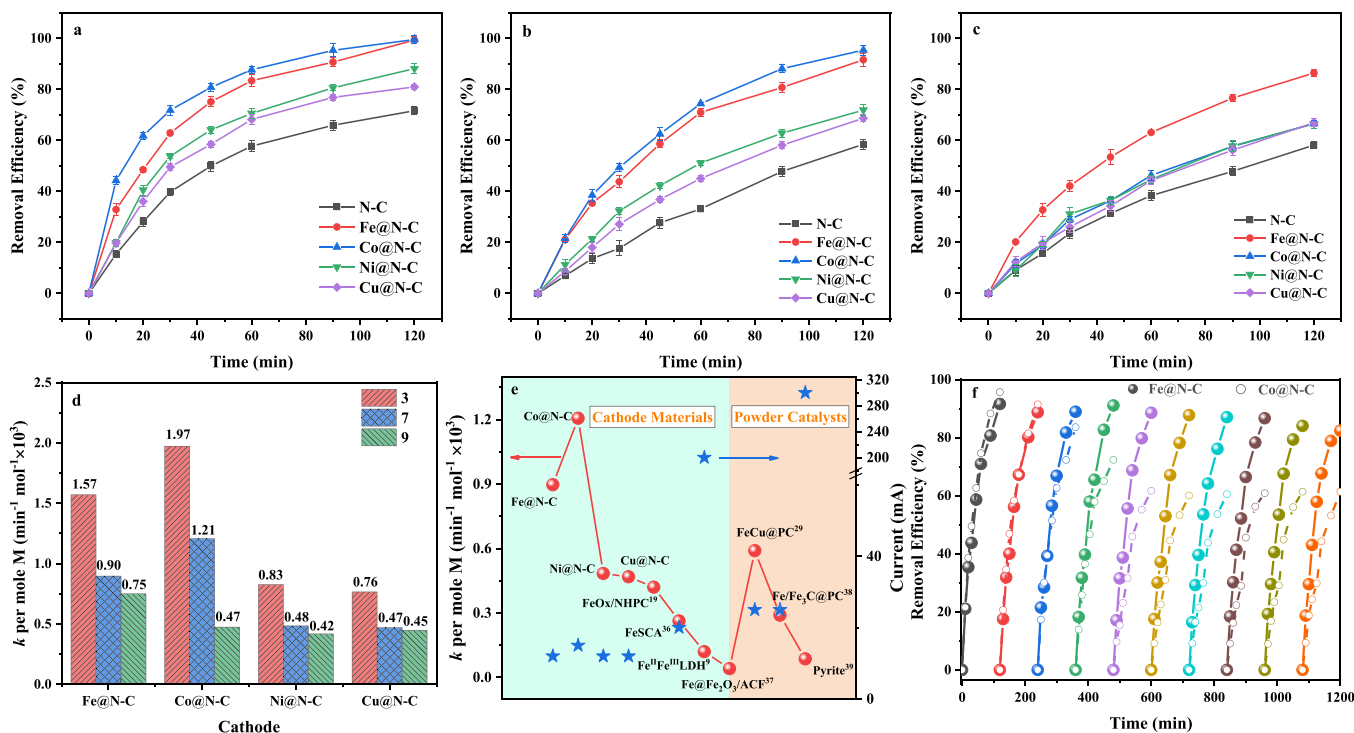

Fig. 4. The SMT degradation by M@N-C and N-C cathode at (a) pH = 3, (b) pH = 7 and (c) pH = 9. Experiment Condition: cathode potential: -0.15 V (vs RHE); catalysts loading: 3 mg cm^{-2}; V: 50 mL; V_{air}: 0.4 L min^{-1}; SMT concentration: 10 mg L^{-1}. (d) the normalized k values by per molar metal atom at different pH; (e) the comparison of applied potential and normalized k values by per molar metal atom at pH = 7 in literatures (The blue ☆ was the applied current); (f) cycling stability of Fe@N-C and Co@N-C cathode for SMT degradation at pH = 7.

utilization of encapsulated metal in M@N-C cathode.

During the SMT degradation, the leaching metal was also important parameter to evaluate the stability of M@N-C cathode. The leaching concentration of metal decreased with the increase of pH (Fig. S16). The leaching Fe at pH = 3 was the highest compared with other metals, reaching 4.03 mg L^{-1}, however, it dramatically dropped to 0.12 mg L^{-1} at pH 7. The leaching Co at pH = 3 and 7 was 2.23 and 0.49 mg L^{-1}, respectively. The corrosion potential of M@N-C was 0.56 V (vs RHE), 0.44 V (vs RHE), 0.52 V (vs RHE) and 0.51 V (vs RHE) at pH = 7, which was consistent with the leaching concentration of metal (Fig. S17). Higher leaching metal would result in higher SMT degradation in homogeneous process (Fig. S18), thus the Fe@N-C would exhibit more potential at neutral and alkaline and Co@N-C had more advantages in acidic environments (Fig. 4c and Table S5). Moreover, the Fe@N-C and Co@N-C could achieve 57.88% and 63.68% TOC removal within 6 h at pH = 7, respectively, which was higher than other M@N-C (Fig. S19).

In order to further explore the superiority of Fe@N-C and Co@N-C cathode, the catalytic stability at pH = 7 by cycling tests was explored (Fig. 4f). It could be seen that a performance declined from 95% to 61% on Co@N-C cathode after 5 cycling tests, after that Co@N-C maintained its catalytic activity. During the cycles of Co@N-C cathode, the leaching Co concentration kept decreasing from 0.49 to 0.13 mg L^{-1} after 10 cycles (Fig. S20), which was below the legal limit of the Industrial Pollutant Emission Standards for Cu, Ni and Co (GB-25467–2010, 1.0 mg L^{-1}). It was amazing that only 10% loss of activity of Fe@N-C cathode after 10 cycles, remaining 82% removal for SMT degradation with around 0.12 mg L^{-1} of Fe leaching at every cycle, which was below the legal limit of the Chinese Drinking Water Hygiene Standard (GB5749–2006, 0.2 mg L^{-1}). Therefore, the Fe@N-C exhibited a higher catalytic stability for SMT degradation compared than that of Co@N-C.

3.4. Generation of reactive species by M@N-C cathode

To explore the reaction pathway and mechanism of M@N-C cathode, the generated reactive species were identified via EPR analysis and quenching experiments in electrocatalytic process. Using DMPO as trapping agent, it could be observed that the nine characteristic peaks of DMPO-H and 1:2:2:1 characteristic peaks of DMPO-OH were simultaneously observed [3], confirming the formation of atomic H* and •OH (Fig. 5a-b), while the intensity of DMPO-H on N-C cathode was very weak. When TEMP was used, the intensity of $^1O_2$ was observed apart from N-C, especially on Fe@N-C cathode exhibiting the highest $^1O_2$ generation (Fig. 5c). The generation of atomic H* and $^1O_2$ followed the sequence of Fe@N-C > Co@N-C > Ni@N-C > Cu@N-C > N-C, indicating that the introduction of metal was conductive to the generation of atomic H* and $^1O_2$. The •OH generation concentration was Co@N-C > Fe@N-C > N-C > Ni@N-C ≈ Cu@N-C. At the same time, the concentration of atomic H* on Fe@N-C cathode was determined to be 28.46 μM via EPR analysis (Fig. S21), which was 1.62-folds, 2.50-folds and 3.64-folds than that on Co@N-C, Ni@N-C and Cu@N-C, respectively [48]. The $^1O_2$ concentration by Fe@N-C cathode was 42.11 μM, which was 2.40-folds, 3.65-folds and 3.76-folds than other M@N-C. The •OH concentration by Co@N-C was 43.14 μM, which was 2.88-folds than Fe@N-C. Ascribed to the strong •OH, the catalytic performance of Co@N-C for SMT degradation was superior than Fe@N-C at pH = 3 and 7 (Fig. 4a-b). However, the generation of •OH was highly depend on pH, and atomic H* and $^1O_2$ have wider pH tolerance, resulting in the Fe@N-C was superior than Co@N-C, which was shown in Fig. 4c-d.

When TBA, MeOH, FFA and BQ was added into the electrolyte to quench the atomic H* and •OH, •OH, $^1O_2$ and $O_2^{•-}$, respectively, the SMT degradation on N-C cathode was shown in Fig. S22. It could be observed that the major radicals produced by N-C cathode were •OH (76%) and other roles (mainly including $O_2^{•-}$). For M@N-C cathode, based on the k value after adding the trapping agent, the role of atomic H* , •OH, $^1O_2$
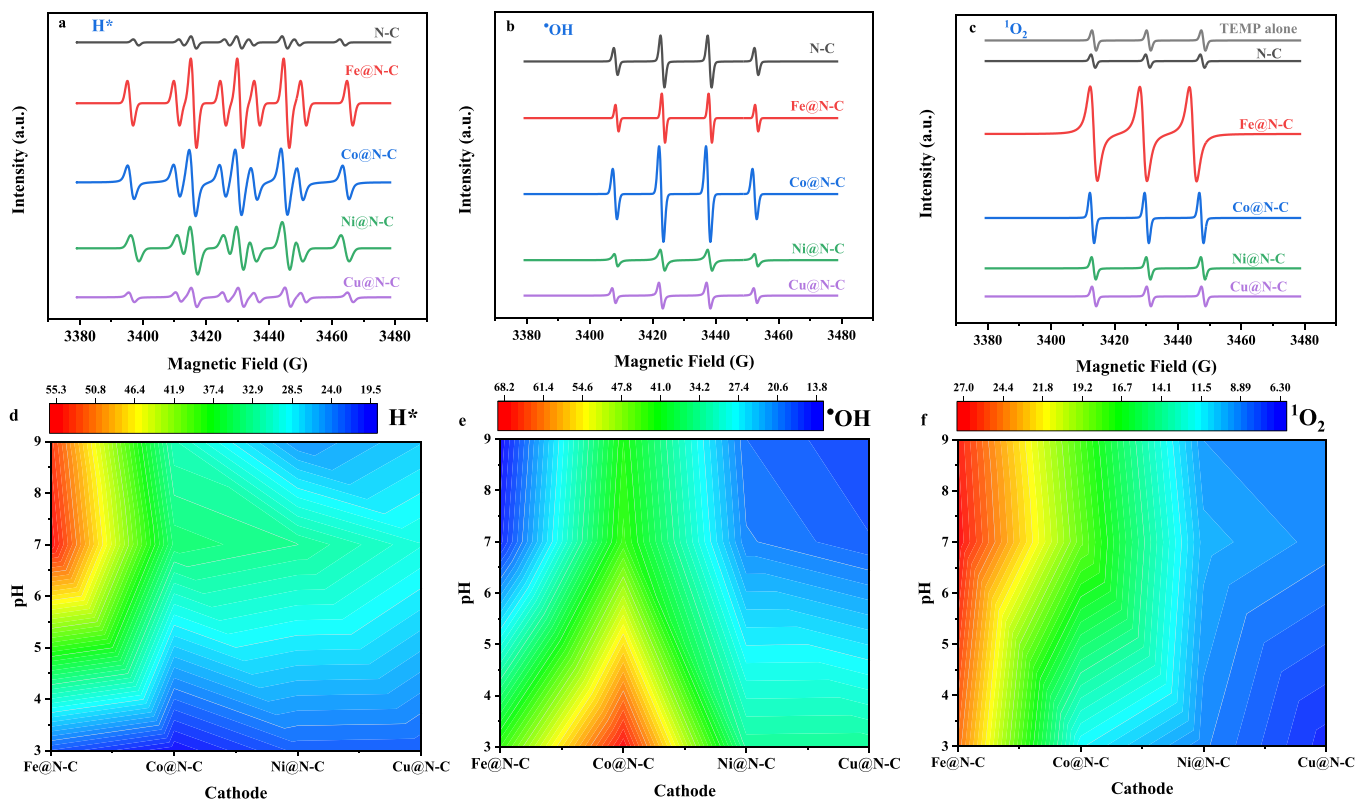
Fig. 5. EPR spectra of (a) DMPO-H* , (b) DMPO-•OH and (c) TEMP-$^1O_2$ by M@N-C and N-C cathode in electrocatalytic process, experimental conditions: DMPO: 100 mM; TEMP: 100 mM; pH: 7; The role of reactive species of (d) atomic H* , (e) •OH, and (f) $^1O_2$ for SMT degradation by M@N-C cathode at different pH.

and $O_2^{\bullet-}$ was calculated and shown in Fig. S23-S26 and Fig. 5d-f. The role of atomic H* at neutral environment was all more prominent than at other conditions (Fig. 4d). On the other hand, the role of $^\bullet$OH was more dominant at acidic solution for all M@N-C, and the overall trend was Co@N-C > Fe@N-C > Ni@N-C > Cu@N-C. The presence of Co was more conductive to promote the generation of $^\bullet$OH, reaching 68% at pH = 3 (Fig. 5e). The responsibility of $^1O_2$ for SMT degradation follow the sequence: Fe@N-C > Co@N-C > Ni@N-C > Cu@N-C at all pH (Fig. 5f), and the $^1O_2$ contribution for SMT removal at neutral and alkaline solution was higher than acidic solution, which exhibited similar trend with atomic H* . It has been reported that the $^1O_2$ and atomic H* was highly pH-independent to 9 [3,18], however, the oxidative ability of $^\bullet$OH sharply decline with the increasing of pH [49], resulting in role of $^\bullet$OH for SMT degradation was lower than catalytic role of $^1O_2$ and atomic H* . Therefore, the SMT was much more degraded at neutral and alkaline solution by Fe@N-C cathode through the role of $^1O_2$ and atomic H* (Fig. 4c). The $O_2^{\bullet-}$ contribution for SMT removal by M@N-C cathode was opposite with $^1O_2$ role (Fig. S27), which also proving that weak conversion of $O_2^{\bullet-}$ to $^1O_2$ in the presence of Ni and Cu, while Fe and Co were more efficiently to convert $O_2^{\bullet-}$ into $^1O_2$. At pH 3, the $^\bullet$OH generation was dominated on all M@N-C cathode, and with the increase of pH, it declined while the atomic H* and $^1O_2$ generation increased.

Overall, the Co@N-C cathode tended to utilize $^\bullet$OH for non-selective oxidation and mineralization of pollutants, especially under acidic conditions. Fe@N-C cathode was more suitable for neutral and alkaline environments, especially under alkaline conditions. Fe@N-C cathode could play a greater role for degradation of pollutants when target pollutant was probes of atomic H* (such as chlorinated organic) [50] and $^1O_2$ (pollutants with electron-rich groups) [51]. If the target pollutants were compounds withdrawing group [52], Ni@N-C and Cu@N-C could degrade the target pollutants more efficiently under alkaline conditions. The above results would provide a guidance for the selectivity between M@N-C cathode via generated reactive species and target pollutants in later research.

To evaluate the ability of forming atomic H* on different cathodes, the energy barrier of atomic H* formation (ΔG_{H*}) was adopted via the DFT calculations. As shown in Fig. 6a, the ΔG_{H*} of N-C was 1.87 eV, and the ΔG_{H*} of M@N-C increased from 0.66 eV to 1.21 eV for Fe@N-C, Co@N-C, Ni@N-C and Cu@N-C, respectively, indicating that Fe@N-C was able to provide more atomic H*. At the same time, the interaction between carbon sites near nitrogen was observed since the *H was adsorbed on the carbon sites near nitrogen sites (Fig. S28). In order to identify the atomic H*, the CV curves of M@N-C were carried out when 2,4-dichlorophenol (2,4-DCP) was added as atomic H* scavenger. As observed in Fig. 6b, the decline of the H*$_{ads}$ (represented H* adsorbed on the catalytic surface) oxidation peak (0.65 V vs RHE) using the Fe@N-C was observed after 2,4-DCP addition, while the peaks of H*$_{abs}$ (represented H* adsorbed in the catalysts crystal lattice) (0.315 V vs RHE) and H$_2$ (−0.395 V vs RHE) appeared. However, the peak of H*$_{ads}$ decreased and peak of H$_2$ generated for N-C and Co@N-C after adding 2,4-DCP (Fig. S29a-S29b). The H*$_{ads}$ and H*$_{abs}$ were observed for Ni@N-C, but disappeared after adding 2,4-DCP and the peak of H$_2$ remained (Fig. S29c). The only H*$_{abs}$ occurred in Cu@N-C (Fig. S29d). The EPR analysis and CV curve confirmed that H*$_{ads}$ rather than H*$_{abs}$ and H$_2$,
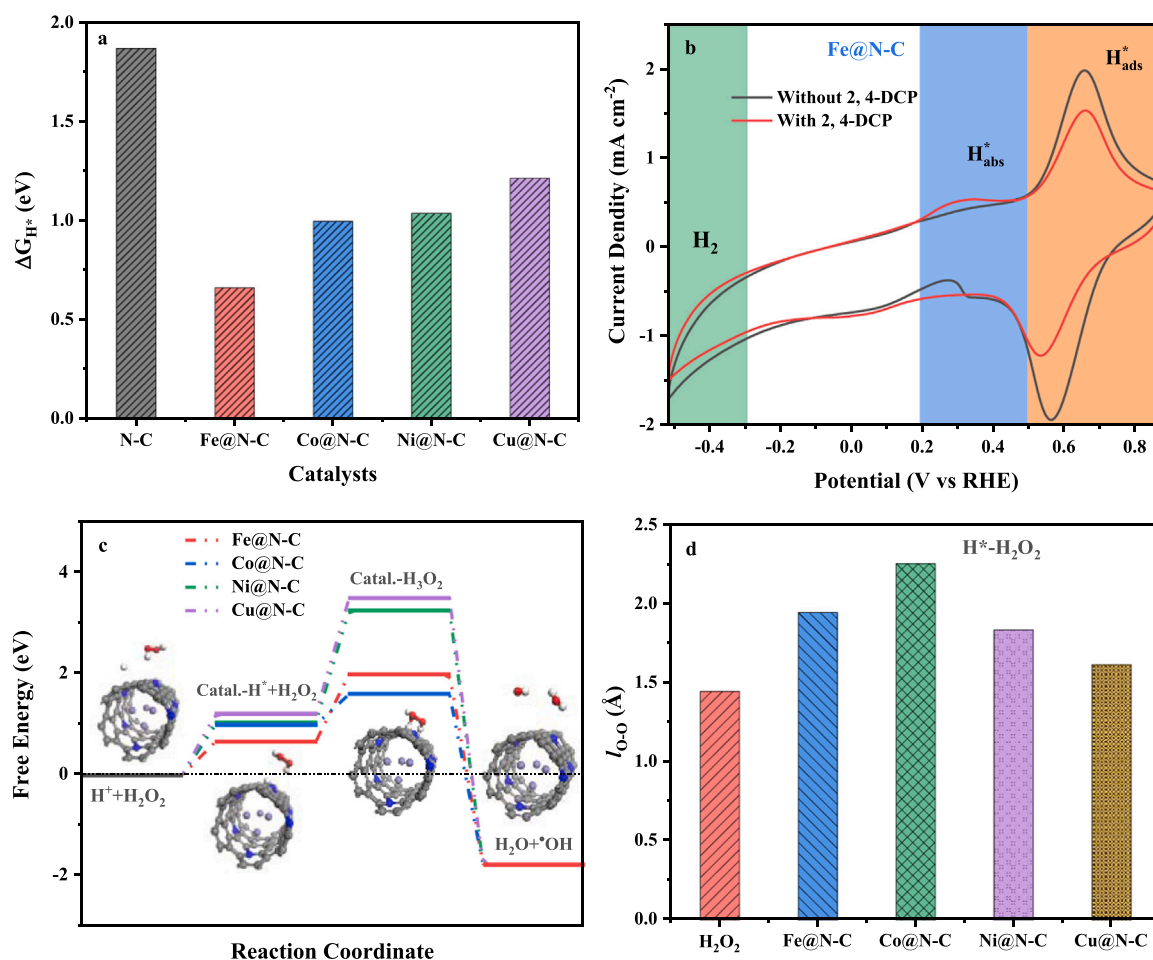

Fig. 6. (a) The energy barrier of atomic H* formation (ΔG_{H*}) as a function of the N-C and M@N-C; (b) CV curves of Fe@N-C with and without 2,4-DCP, 2.4-DCP: 10 mg L^{-1}; (c) Free energy change of the atomic H* -initiated H$_2$O$_2$ in electrocatalytic process on surface of M@N-C; (d) O-O bond (l_{O-O}) of the H$_2$O$_2$ and Cata.-H* - H$_2$O$_2$ adduct.

was the key to active species on M@N-C cathode, especially Fe@N-C. With the addition of H_2O_2, the oxidation peak for H^*_{ads} or H^*_{abs} was declined mainly due to the fact that H_2O_2 scavenged H^*_{ads} or H^*_{abs} (Fig. S30). Therefore, atomic H* could efficiently trigger the conversion of H_2O_2.

It has been reported that the atomic H* could react with H_2O_2 to generate •OH, and the catalysts-H_3O_2 (Cata.-H_3O_2) was a combination of atomic H* on the M@N-C surface and H_2O_2 [3], which was critical intermediate in the generation of •OH via Eq.(1). The process of •OH generation via atomic H* activated H_2O_2 was elucidated by DFT calculated. The free energy diagrams of the atomic H* -H_2O_2 process on the surface of M@N-C catalysts were shown in Fig. 6c. Due to the favorable bonding of atomic H* on the M@N-C surface, only the energy barrier of 1.60 eV was required for formation of the Co@N-C-H_3O_2 adduct, and next was 2.00 eV for Fe@N-C-H_3O_2. In a subsequent step, a negative energy of − 1.77 eV was for •OH generation via electron transfer between atomic H* and H_2O_2. The O-O bond (l_{O-O}) of the Cata.-H* -H_2O_2 adduct was lengthened from 1.45 Å in H_2O_2 to 1.95 Å in Fe@N-C-H* -H_2O_2 and 2.26 Å in Co@N-C-H* -H_2O_2 (Fig. 6d), indicating that the cleavage of the O-O bond in the H* -H_2O_2 adduct accompanied with the formation of •OH and H_2O. Therefore, the Co@N-C was favorable to generate •OH via atomic H* activation of H_2O_2, which was consistent with EPR analysis. Although the Fe@N-C cathode was more conductive to generate atomic H* (Fig. 6a), the ability of H_2O_2 conversion through the role of atomic H* to generate •OH was weak. However, the more $^1O_2$ and atomic H* contribution to SMT removal on Fe@N-C cathode was obtained at alkaline environment (Fig. 5f).

$$H* + H2O2 \rightarrow •OH + H2O \tag{1}$$

3.5. Catalytic mechanism of M@N-C for pollutants degradation

The mechanism of M@N-C cathode for pollutants degradation must be considered in electrocatalytic process. The key intermediates during electrocatalytic process by M@N-C was identified via in-situ FITR (Fig. 7). The absorbance peaks for N-C at 1400, 2343, 3239 and 3455 cm^{-1} increased with the increasing of potential, which attributed to the adsorption of O_2 (O_2 *), CO_2, -OH group and -NH_2 group [53–56], respectively (Fig. 7a). This indicated that O_2 was first adsorbed to initiate H_2O_2 generation and the -NH_2 group appeared after ORR, supporting the role of N for catalytic process [57]. Also -OH group was involved in the SMT degradation, suggesting the participation of •OH and thus SMT was further mineralized to CO_2. At the same time, the CH/CH_2 group (2379 cm^{-1}, 2892 cm^{-1} and 2985 cm^{-1}) [58,59] also formed with the decrease of potential. For Fe@N-C, the absorbance peaks of O_2*, CO_2 and -OH group were also observed with the increase of potential, and the peak intensity of CO_2 was higher than that of N-C, indicating that SMT degradation was more effective on Fe@N-C than N-C (Fig. 4b). It was important that the CH-groups of pyridinic ring (3134 cm^{-1}) [60] increased with the decline of potential, which was belonged to the generation of atomic H* due to activity sites for H* production was the carbon sites near nitrogen (Fig. S28). With the increase of potential, the C=N bond (1652 cm^{-1}) [61] gradually declined and finally disappeared at − 0.25 V (vs RHE). The peak of C-N (1139 cm^{-1}) [62] bond also weakened, proving that the pyridinic N and graphite N participated in the electrocatalytic process. However, the C=N bond appeared and C-N bond strengthened first and then weakened on Co@N-C, indicating that the role of graphite N was dominant (Fig. 7c). The C=N and C-N bond was not observed from Ni@N-C and Cu@N-C (Fig. 7d-e). There were more CH/CH_2 group on the Co@N-C, Ni@N-C and Cu@N-C catalyst, resulting in less generation of atomic H* (Fig. 7b-e). The intensity of CO_2 peak for all M@N-C was consistent with SMT and TOC removal. In-situ FITR spectra of electrocatalytic process on Fe@N-C and Co@N-C cathode at − 0.15 V (vs RHE) was observed (Fig. 8a-b), indicating that Fe@N-C and Co@N-C was stable for SMT removal in electrocatalytic process.

The pathway and key intermediates of H_2O_2 generation were also explored in the absence of SMT via in-situ FITR on Fe@N-C and Co@N-C compared with catalytic process (Fig. 8c-d). In ORR process, the peak of C=N bond was not is unchanged, proving the pyridinic N was not participated in ORR. And the intensity of C=N bond in Co@N-C was higher than Fe@N-C, proving that Co@N-C exhibited the stronger ORR process due to the pyridinic N was generated after ORR [57], which was
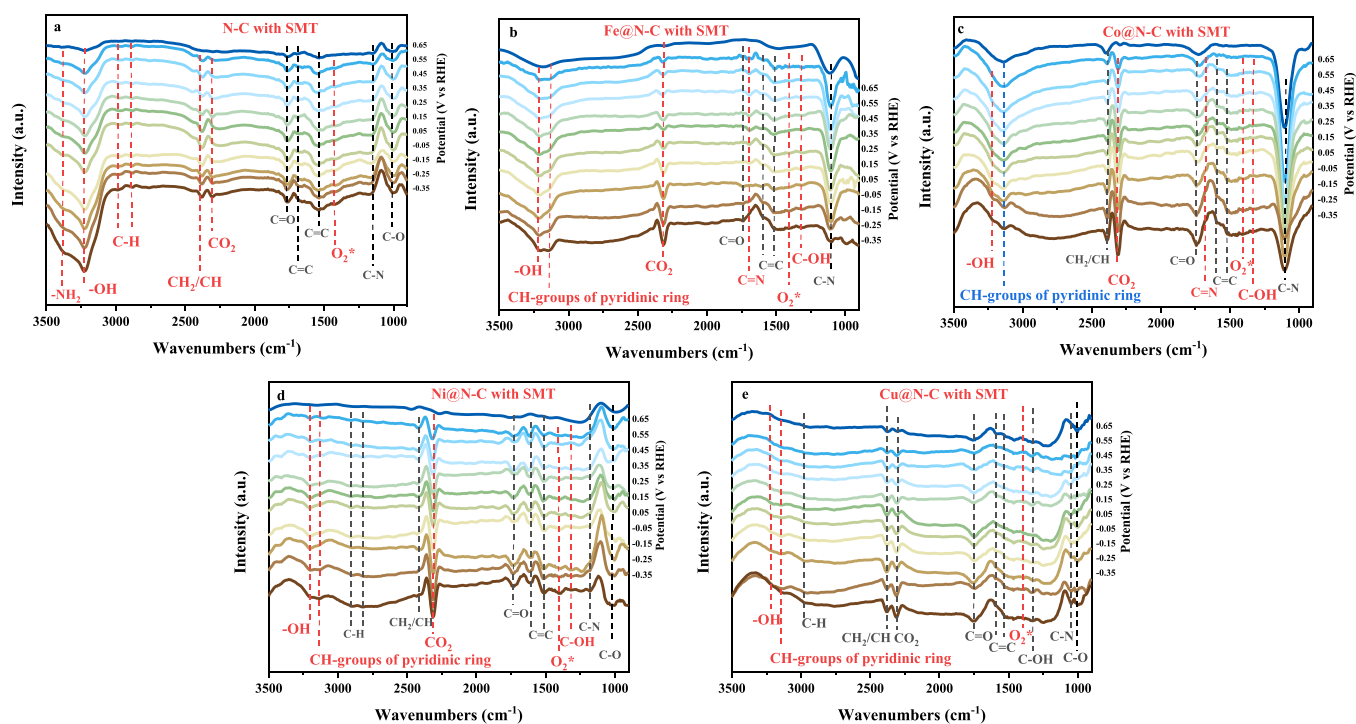

Fig. 7. In-situ FITR spectra of electrocatalytic process on (a) N-C, (b) Fe@N-C, (c) Co@N-C, (d) Ni@N-C and (e) Co@N-C with SMT (10 mg L^{-1}) under the potential from 0.65 to − 0.35 V (vs RHE) at O_2-saturated Na_2SO_4 solutions (50 mM, pH =7), respectively.
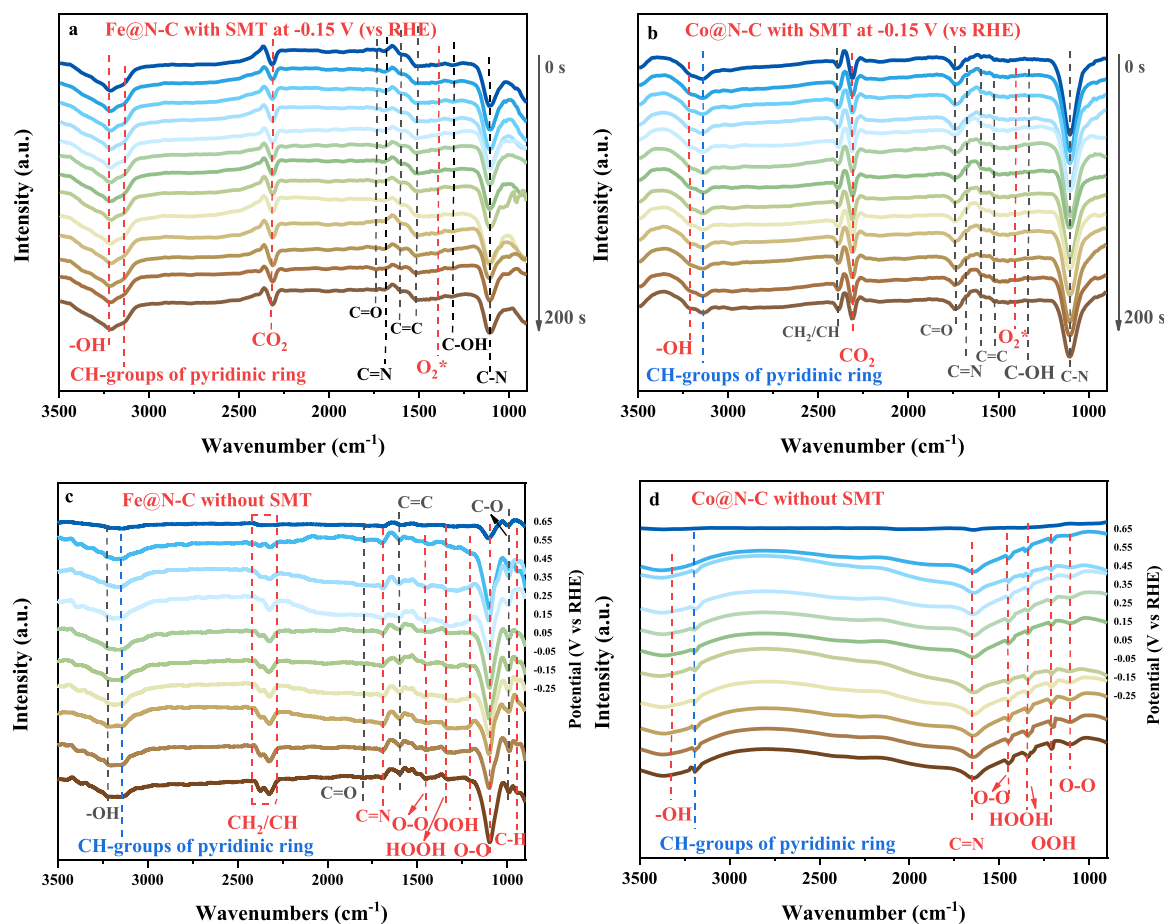
Fig. 8. In-situ FITR spectra of electrocatalytic process on (a) Fe@N-C and (b) Co@N-C with SMT (10 mg L^{-1}) at − 0.15 V (vs RHE); in-situ FITR spectra on (c) Fe@N-C and (d) Co@N-C without SMT under the potential from 0.65 to − 0.35 V (vs RHE). The electrolyte was O$_2$-saturated Na$_2$SO$_4$ solutions.

consistent with Fig. 2. The C-N bond was not observed, however, the O-O stretching vibration at 1095 cm^{-1} was observed, assigning to species such as HO$_2$ or O$_2^-$ or H$_2$O$_2$ and weakly adsorbed O$_2$, respectively [63,64]. Although the O-O bond on Co@N-C was higher than that on Fe@N-C, the peak at 1212 cm^{-1} and 1386 cm^{-1} attributed to the OOH and HOOH [63], proving more H$_2$O$_2$ generation on the surface of Co@N-C than Fe@N-C. It was important to note that the CH-groups of pyridinic ring was also generated for ORR process. Compared with catalytic process for SMT degradation, -OH group was less as shown in Fig. 7b-c.

These results of in-situ FTIR further verified that the pyridinic N and graphite N both participated in the electrocatalytic process on Fe@N-C, but the more graphite N was involved on Co@N-C. And the generation of atomic H* was related to the CH-group in the M@N-C structure, resulting in more atomic H* generation. The more •OH generation would lead to the faster pollutant degradation, and further deep mineralization ascribed to more CO$_2$ formation.

3.6. The application prospect of M@N-C cathode

Various pollutants (phenol, tetracycline (TC), rhodamine B (Rh B) and methylene blue (MB)) degradation by N-C and M@N-C cathode at pH 7 was shown in Fig. S31 to further explore the activity trend, observing the degradation by M@N-C was improved compared with N-C and the trend by M@N-C was Co@N-C > Fe@N-C > Ni@N-C > Cu@N-C (Fig. 9a). The EEC of SMT and phenol degradation by Fe@N-C cathode was both lower than Co@N-C, however, the Co@N-C cathode was more cost-effective for TC, Rh B and MB. EEC of various pollutants degradation was lower than 0.8 kWh•log^{-1}•m^{-3}, which was more cost-effective,

especially in Fe@N-C and Co@N-C cathode (Fig. 9b and Table S5).

In order to evaluate the catalytic performance of M@N-C cathode (Fe@N-C and Co@N-C was taken as the representative example) in electrocatalytic process, three real wastewater (Mati lake, industrial wastewater effluent and pharmaceutical wastewater, and their quality parameters were shown in Table S6) was chosen (Fig. 9c). It could be observed that the SMT degradation in three real wastewater by Fe@N-C cathode was similar with that the simulated wastewater, reaching about 92%. However, the SMT removal decreased by Co@N-C cathode decreased to 72.91%, 80.10% and 88.40% in above real wastewater compared with simulated wastewater (95.37%), respectively, due to the pH was 8.52, 8.11 and 7.58. This comparison confirmed that the Fe@N-C cathode had wider pH range adaptability compared with Co@N-C (also shown in Fig. 3c for SMT removal) possibly due to the inherent nature of atomic H* and ^{1}O$_2$, which would not need to adjust pH before treatment to reduce treatment cost.

4. Conclusions

The M@N-C (M: Fe, Co, Ni and Cu) with similar structural and physiochemical properties were exploited as bifunctional cathode to achieve high H$_2$O$_2$ selectivity and efficient degradation of pollutants, uncovering their activity trends in electrocatalytic process. Co was more conductive to H$_2$O$_2$ generation than Fe via DFT calculation and in-situ FITR observation at neutral and alkaline environments in the role of graphite N (Co@N-C > Fe@N-C > N-C > Ni@N-C > Cu@N-C), however, the more -COOH group enhanced the higher H$_2$O$_2$ generation on Fe@N-C at acidic environments. The activity order for SMT degradation was Co@N-C (1.21 ×10^3 min^{-1} mol^{-1} per mole Co atom sites) > Fe@N-C
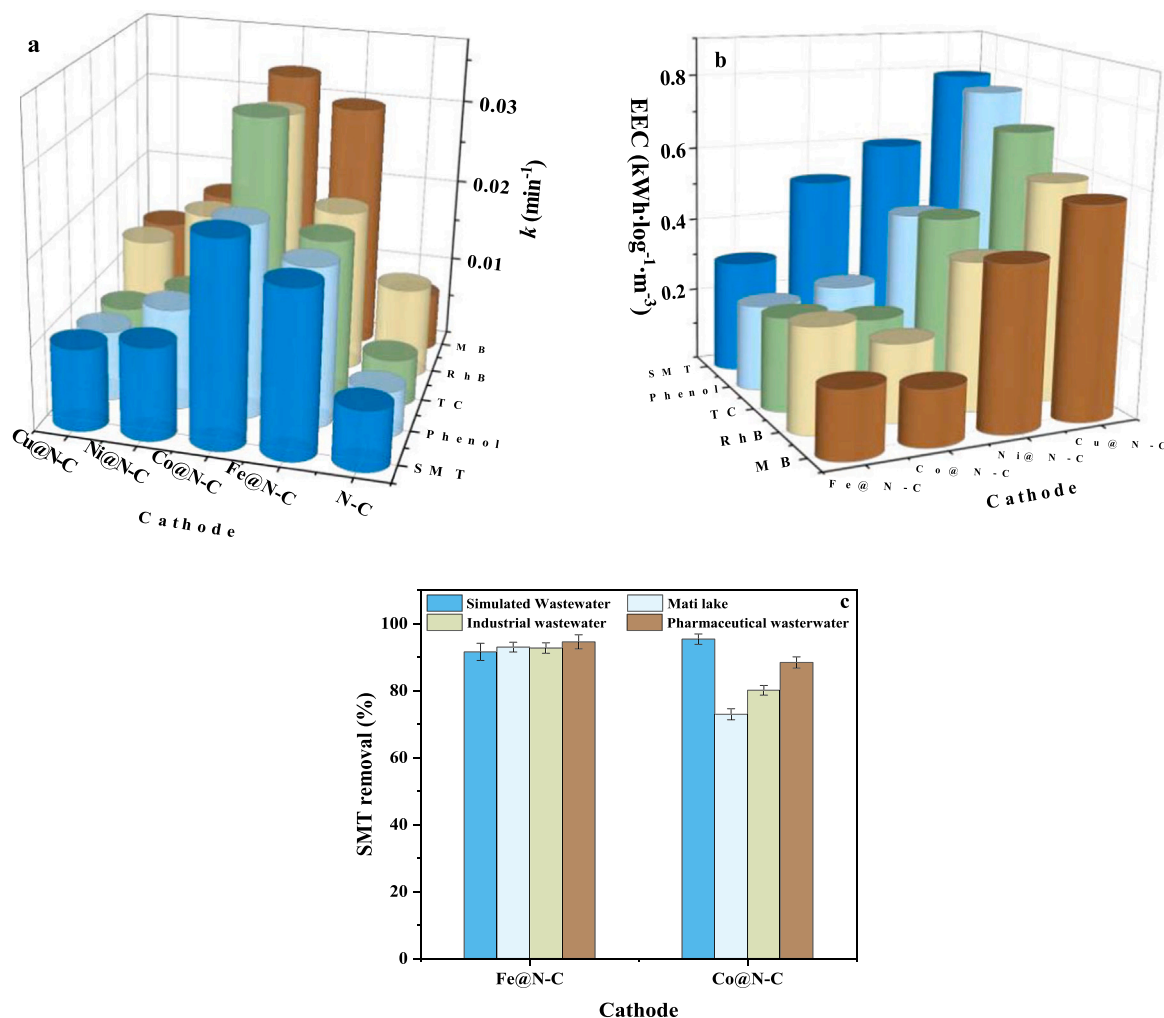
Fig. 9. (a) the rate constant (k) and (b) EEC of various pollutants (10 mg L^{-1}) degradation by N-C and M@N-C cathode at pH = 7; (c) SMT degradation in the simulated wastewater, Mati lake, industrial wastewater effluent and pharmaceutical wastewater in electrocatalytic process of Fe@N-C and Co@N-C cathode.

> Ni@N-C > Cu@N-C at neutral environment, with high metal active site utilization of encapsulated metal. A highly reactive, green and stable M@N-C cathode was screened through synchronous role for atomic H*, $^{\bullet}$OH, $^{1}O_2$ and $O_2^{\bullet-}$, especially in Fe@N-C and Co@N-C with EEC lower than 0.5 kWh$\cdot$log$^{-1}\cdot$m^{-3}. Co was more conductive to generate $^{\bullet}$OH (contribution up to 68%) via atomic H* as H_2O_2 activator for pollutants degradation by the green electrochemical process at acidic solution. While Fe was more conductive to generate atomic H* (contribution of 55%) at wider pH range to 9 through the role of pyridinic N, exhibiting more potential in stability and reusability with lower leaching Fe (0.12 mg L^{-1} for 10 cycles) and similar treatment effectiveness both in simulated wastewaters and real wastewaters (Mati lake, industrial wastewater and pharmaceutical wastewater). Overall, this study not only gained insight into the catalytic mechanism of N-doping CNTs encapsulated transition metal cathode in electrocatalytic process but also offered new guidance towards various pollutants degradation via selection of M@N-C due to different active species formation.

CRediT authorship contribution statement

Pei Su: Conceptualization, Methodology, Formal analysis, Investigation, Data curation, Writing – original draft, Writing – review & editing. **Wenyang Fu:** Investigation, Resources, Data curation. **Zhongzheng Hu and Jiana Jing:** Data curation. **Minghua Zhou:** Conceptualization, Supervision, Funding acquisition, Resources, Writing – review & editing.

Declaration of Competing Interest

The authors declare that they have no known competing financial interests or personal relationships that could have appeared to influence the work reported in this paper.

Acknowledgments

Appendix A. Supporting information

Supplementary data associated with this article can be found in the online version at doi:10.1016/j.apcatb.2022.121457.

References

[1] Y.M. Liu, S. Chen, X. Quan, H.T. Yu, H.M. Zhao, Y.B. Zhang, Efficient mineralization of perfluorooctanoate by electro-Fenton with H_2O_2 electro-generated on hierarchically porous carbon, Environ. Sci. Technol. 49 (2015) 13528–13533.

[2] H.W. Sun, F. He, W.Y. Choi, Production of reactive oxygen species by the reaction of periodate and hydroxylamine for rapid removal of organic pollutants and waterborne bacteria, Environ. Sci. Technol. 54 (2020) 6427–6437.

[3] H.B. Zeng, G. Zhang, Q.H. Ji, H.J. Liu, X. Hua, H.L. Xia, M. Sillanpaa, J.H. Qu, pH-independent production of hydroxyl radical from atomic H*-mediated electrocatalytic H_2O_2 reduction: a green Fenton process without byproducts, Environ. Sci. Technol. 54 (2020) 14725–14731.

[4] Q. Zhang, M. Zhou, G. Ren, Y. Li, Y. Li, X. Du, Highly efficient electrosynthesis of hydrogen peroxide on a superhydrophobic three-phase interface by natural air diffusion, Nat. Commun. 11 (2020) 1731.

[5] X. Du, S. Wang, F. Ye, Z. Qingrui, Derivatives of metal-organic frameworks for heterogeneous Fenton-like processes: from preparation to performance and mechanisms in wastewater purification - a mini review, Environ. Res. 206 (2022), 112414.

[6] D.N. Pei, C. Liu, A.Y. Zhang, X.Q. Pan, H.Q. Yu, In situ organic Fenton-like catalysis triggered by anodic polymeric intermediates for electrochemical water purification, Proc. Natl. Acad. Sci. U.S.A. 117 (2020) 30966–30972.

[7] P.V. Nidheesh, R. Gandhimathi, Trends in electro-Fenton process for water and wastewater treatment: An overview, Desalination 299 (2012) 1–15.

[8] P. Cao, X. Quan, K. Zhao, S. Chen, H. Yu, Y. Su, High-efficiency electrocatalysis of molecular oxygen toward hydroxyl radicals enabled by an atomically dispersed iron catalyst, Environ. Sci. Technol. 54 (2020) 12662–12672.

[9] P. Su, X. Du, Y. Zheng, W. Fu, Q. Zhang, M. Zhou, Interface-confined multi-layered reaction centers between Ce-MOFs and $Fe_3O_4@C$ for heterogeneous electro-Fenton at wide pH 3–9: Mediation of Ce^{3+}/Ce^{4+} and oxygen vacancy, Chem. Eng. J. (2021) 133597.

[10] P. Cao, X. Quan, K. Zhao, S. Chen, H. Yu, J. Niu, Selective electrochemical H_2O_2 generation and activation on a bifunctional catalyst for heterogeneous electro-Fenton catalysis, J. Hazard. Mater. 382 (2020) 121102.

[11] D. Guo, Y. Liu, H. Ji, C.C. Wang, B. Chen, C. Shen, F. Li, Y. Wang, P. Lu, W. Liu, Silicate-enhanced heterogeneous flow-through electro-Fenton system using iron oxides under nanoconfinement, Environ. Sci. Technol. 55 (2021) 4045–4053.

[12] W.L. Yang, M.H. Zhou, L. Mai, H. Ou, N. Oturan, M.A. Oturan, E.Y. Zeng, Generation of hydroxyl radicals by metal-free bifunctional electrocatalysts for enhanced organics removal, Sci. Total Environ. 791 (2021), 148107.

[13] Y.Y. Sun, I. Sinev, W. Ju, A. Bergmann, S. Dresp, S. Kuhl, C. Spori, H. Schmies, H. Wang, D. Bernsmeier, B. Paul, R. Schmack, R. Kraehnert, B. Roldan Cuenya, P. Strasser, Efficient electrochemical hydrogen peroxide production from molecular oxygen on nitrogen-doped mesoporous carbon catalysts, ACS Catal. 8 (2018) 2844–2856.

[14] P. Su, M.H. Zhou, X.Y. Lu, W.L. Yang, G.B. Ren, J.J. Cai, Electrochemical catalytic mechanism of N-doped graphene for enhanced H_2O_2 yield and in-situ degradation of organic pollutant, Appl. Catal. B-Environ. 245 (2019) 583–595.

[15] M.R. Haider, W.L. Jiang, J.L. Han, H.M.A. Sharif, Y.C. Ding, H.Y. Cheng, A. J. Wang, In-situ electrode fabrication from polyaniline derived N-doped carbon nanofibers for metal-free electro-Fenton degradation of organic contaminants, Appl. Catal. B-Environ. 256 (2019), 117774.

[16] W.L. Yang, M.H. Zhou, L. Liang, Highly efficient in-situ metal-free electrochemical advanced oxidation process using graphite felt modified with N-doped graphene, Chem. Eng. J. 338 (2018) 700–708.

[17] H. Ghanbarlou, B. Nasernejad, M.N. Fini, M.E. Simonsen, J. Muff, Synthesis of an iron-graphene based particle electrode for pesticide removal in three-dimensional heterogeneous electro-Fenton water treatment system, Chem. Eng. J. 395 (2020), 125025.

[18] Z.C. Yang, J.S. Qian, A.Q. Yu, B.C. Pan, Singlet oxygen mediated iron-based Fenton-like catalysis under nanoconfinement, Proc. Natl. Acad. Sci. U.S.A. 116 (2019) 6659–6664.

[19] P. Cao, K. Zhao, X. Quan, S. Chen, H. Yu, Efficient and stable heterogeneous electro-Fenton system using iron oxides embedded in Cu, N co-doped hollow porous carbon as functional electrocatalyst, Sep. Purif. Technol. 238 (2020), 116424.

[20] H.-C. Li, X.-Y. Ji, X.-Q. Pan, C. Liu, W.-J. Liu, Ionothermal carbonization of biomass to construct Fe, N-doped biochar with prominent activity and recyclability as cathodic catalysts in heterogeneous electro-Fenton, ACS EST Eng. 1 (2020) 21–31.

[21] K. Liu, J.C.C. Yu, H. Dong, J.C.S. Wu, M.R. Hoffmann, Degradation and mineralization of carbamazepine using an electro-Fenton reaction catalyzed by magnetite nanoparticles fixed on an electrocatalytic carbon fiber textile cathode, Environ. Sci. Technol. 52 (2018) 12667–12674.

[22] Y.M. Liu, X. Quan, X.F. Fan, H. Wang, S. Chen, High-yield electrosynthesis of hydrogen peroxide from oxygen reduction by hierarchically porous carbon, Angew. Chem. Int. Ed. 54 (2015) 6837–6841.

[23] S. Ammar, M.A. Oturan, L. Labiadh, A. Guersalli, R. Abdelhedi, N. Oturan, E. Brillas, Degradation of tyrosol by a novel electro-Fenton process using pyrite as heterogeneous source of iron catalyst, Water Res. 74 (2015) 77–87.

[24] L.M. Dai, Y.H. Xue, L.T. Qu, H.J. Choi, J.B. Baek, Metal-free catalysts for oxygen reduction reaction, Chem. Rev. 115 (2015) 4823–4892.

[25] G.D. Gao, Q.Y. Zhang, Z.W. Hao, C.D. Vecitis, Carbon nanotube membrane stack for flow-through sequential regenerative electro-Fenton, Environ. Sci. Technol. 49 (2015) 2375–2383.

[26] W.P. Xiong, G.M. Zeng, Z.H. Yang, Y.Y. Zhou, C. Zhang, M. Cheng, Y. Liu, L. Hu, J. Wan, C.Y. Zhou, R. Xu, X. Li, Adsorption of tetracycline antibiotics from aqueous solutions on nanocomposite multi-walled carbon nanotube functionalized MIL-53 (Fe) as new adsorbent, Sci. Total Environ. 627 (2018) 235–244.

[27] C. Zhang, C. Lai, G.M. Zeng, D.L. Huang, C.P. Yang, Y. Wang, Y.Y. Zhou, M. Cheng, Efficacy of carbonaceous nanocomposites for sorbing ionizable antibiotic sulfamethazine from aqueous solution, Water Res. 95 (2016) 103–112.

[28] J.T. Tang, J.L. Wang, MOF-derived three-dimensional flower-like FeCu@C composite as an efficient Fenton-like catalyst for sulfamethazine degradation, Chem. Eng. J. 375 (2019).

[29] L. Zhang, Y. Wang, P. Su, R. Mao, J. Zhao, Photo-electrocatalytic degradation of chlorinated organics via atomic hydrogen reduction and hydroxyl radical oxidation by Fe and P co-doped carbon aerogel cathode, J. Clean. Prod. 298 (2021), 126808.

[30] D.H. Deng, L. Yu, X.Q. Chen, G.X. Wang, L. Jin, X.L. Pan, J. Deng, G.Q. Sun, X. H. Bao, Iron encapsulated within pod-like carbon nanotubes for oxygen reduction reaction, Angew. Chem. Int. Ed. 52 (2013) 371–375.

[31] Y. Wang, N. Ren, J. Xi, Y. Liu, T. Kong, C. Chen, Y. Xie, X. Duan, S. Wang, Mechanistic investigations of the pyridinic N–Co structures in Co embedded N-doped carbon nanotubes for catalytic ozonation, ACS EST Eng. 1 (2021) 32–45.

[32] X. Du, W. Fu, P. Su, J. Cai, M. Zhou, Internal-micro-electrolysis-enhanced heterogeneous electro-Fenton process catalyzed by $Fe/Fe_3C@PC$ core–shell hybrid for sulfamethazine degradation, Chem. Eng. J. 398 (2020), 125681.

[33] H. Zhao, L. Qian, Y. Chen, Q. Wang, G. Zhao, Selective catalytic two-electron O_2 reduction for onsite efficient oxidation reaction in heterogeneous electro-Fenton process, Chem. Eng. J. 332 (2018) 486–498.

[34] M. Bhaumik, A. Maity, H.G. Brink, Zero valent nickel nanoparticles decorated polyaniline nanotubes for the efficient removal of Pb(II) from aqueous solution: Synthesis, characterization and mechanism investigation, Chem. Eng. J. 417 (2021), 127910.

[35] M.J. Huang, H.H. Chen, J. He, J.N. Chen, L.N. Sun, Y.L. Li, X.Z. Ren, L.B. Deng, Synthesis of ultrathin $MoS(2)$nanosheets embedded in 3D hierarchically nitrogen-and-sulfur Co-doped porous carbon composites as efficient oxygen reduction reaction catalyst, Chemelectrochem 7 (2020) 3260–3268.

[36] Y.J. Yao, H. Chen, J.C. Qin, G.D. Wu, C. Lian, J. Zhang, S.B. Wang, Iron encapsulated in boron and nitrogen codoped carbon nanotubes as synergistic catalysts for Fenton-like reaction, Water Res. 101 (2016) 281–291.

[37] W. Sang, C. Wang, X. Zhang, X. Yu, C. Yu, J. Zhao, X. Wang, X. Yang, L. Li, Dendritic $Co_{0.52}Cu_{0.48}$ and $Ni_{0.19}Cu_{0.81}$ alloys as hydrogen generation catalysts via hydrolysis of ammonia borane, Int. J. Hydrog. Energ. 42 (2017) 30691–30703.

[38] X. Du, W. Fu, P. Su, L. Su, Q. Zhang, J. Cai, M. Zhou, Trace FeCu@PC derived from MOFs for ultraefficient heterogeneous electro-Fenton process: enhanced electron transfer and bimetallic synergy, ACS EST Eng. 1 (2021) 1311–1322.

[39] Y. Wu, X. Chen, Y. Han, D. Yue, X. Cao, Y. Zhao, X. Qian, Highly efficient utilization of nano-Fe(0) embedded in mesoporous carbon for activation of peroxydisulfate, Environ. Sci. Technol. 53 (2019) 9081–9090.

[40] Z. Fan, J. Li, W. Yang, Q. Fu, K. Sun, Y.-C. Song, Z. Wei, Q. Liao, X. Zhu, Green and facile synthesis of iron oxide nanoparticle-embedded N-doped biocarbon as an efficient oxygen reduction electrocatalyst for microbial fuel cells, Chem. Eng. J. 385 (2020), 123393.

[41] H. Zhao, X. Shen, Y. Chen, S.N. Zhang, P. Gao, X. Zhen, X.H. Li, G. Zhao, A COOH-terminated nitrogen-doped carbon aerogel as a bulk electrode for completely selective two-electron oxygen reduction to H_2O_2, Chem. Commun. 55 (2019) 6173–6176.

[42] Q.R. Zhang, X. Tan, N.M. Bedford, Z.J. Han, L. Thomsen, S. Smith, R. Amal, X. Y. Lu, Direct insights into the role of epoxy groups on cobalt sites for acidic H_2O_2 production, Nat. Commun. 11 (2020) 4181.

[43] S. Siahrostami, A. Verdaguer-Casadevall, M. Karamad, D. Deiana, P. Malacrida, B. Wickman, M. Escudero-Escribano, E.A. Paoli, R. Frydendal, T.W. Hansen, I. Chorkendorff, I.E.L. Stephens, J. Rossmeisl, Enabling direct H_2O_2 production through rational electrocatalyst design, Nat. Mater. 12 (2013) 1137–1143.

[44] C. Liu, H. Li, F. Liu, J.S. Chen, Z.X. Yu, Z.W. Yuan, C.J. Wang, H.L. Zheng, G. Henkelman, L. Wei, Y. Chen, Intrinsic activity of metal centers in metal-nitrogen-carbon single-atom catalysts for hydrogen peroxide synthesis, J. Am. Chem. Soc. 142 (2020) 21861–21871.

[45] Q. Tian, F. Xiao, H. Zhao, X. Fei, X. Shen, G. Postole, G. Zhao, Simultaneously accelerating the regeneration of FeII and the selectivity of 2e⁻ oxygen reduction over sulfide iron-based carbon aerogel in electro-Fenton system, Appl. Catal. B-Environ. 272 (2020), 119039.

[46] J.P. Li, Z.H. Ai, L.Z. Zhang, Design of a neutral electro-Fenton system with Fe@ Fe_2O_3/ACF composite cathode for wastewater treatment, J. Hazard. Mater. 164 (2009) 18–25.

[47] N. Barhoumi, N. Oturan, S. Ammar, A. Gadri, M.A. Oturan, E. Brillas, Enhanced degradation of the antibiotic tetracycline by heterogeneous electro-Fenton with pyrite catalysis, Environ. Chem. Lett. 15 (2017) 689–693.

[48] V. Krishna, D. Yanes, W. Imaram, A. Angerhofer, B. Koopman, B. Moudgil, Mechanism of enhanced photocatalysis with polyhydroxy fullerenes, Appl. Catal. B-Environ. 79 (2008) 376–381.

[49] G.V. Buxton, C.L. Greenstock, W.P. Helman, A.B. Ross, Critical review of rate constants for reactions of hydrated electrons, hydrogen atoms and hydroxyl radicals (˙OH/˙O- in aqueous solution, J. Phys. Chem. Ref. Data 17 (1988) 513–886.

[50] J. Zhang, G. Zhang, H. Lan, J. Qu, H. Liu, Synergetic hydroxyl radical oxidation with atomic hydrogen reduction lowers the organochlorine conversion barrier and potentiates effective contaminant mineralization, Environ. Sci. Technol. 55 (2021) 3296–3304.

[51] Z. Yang, J. Qian, C. Shan, H. Li, Y. Yin, B. Pan, Toward selective oxidation of contaminants in aqueous systems, Environ. Sci. Technol. 55 (2021) 14494–14514.

[52] Y. Guo, J. Zhan, G. Yu, Y. Wang, Evaluation of the concentration and contribution of superoxide radical for micropollutant abatement during ozonation, Water Res. 194 (2021), 116927.

[53] E.G. Sorte, D.-J. Chen, Y.J. Tong, Dual-electrode in situ infrared spectroscopy for fuel cells, J. Electrochem. Soc. 163 (2015) H3038–H3042.

[54] R. Vargas, C. Borrás, D. Plana, J. Mostany, B.R. Scharifker, Kinetic study of the electrochemical mineralization of phenols in thin-layer condition, Electrochim. Acta 55 (2010) 6501–6506.

[55] H. Liu, G. Zhang, Y. Zhou, M. Gao, F. Yang, One-step potentiodynamic synthesis of poly(1,5-diaminoanthraquinone)/reduced graphene oxide nanohybrid with improved electrocatalytic activity, J. Mater. Chem. A 1 (2013) 13902.

[56] A. Romero, M.P. Lavín-López, A.R. de la Osa, S. Ordoñez, A. de Lucas-Consuegra, J. L. Valverde, A. Patón, Different strategies to simultaneously N-doping and reduce graphene oxide for electrocatalytic applications, J. Electroanal. Chem. 857 (2020), 113695.

[57] P. Su, M. Zhou, G. Song, X. Du, X. Lu, Efficient H_2O_2 generation and spontaneous ·OH conversion for in-situ phenol degradation on nitrogen-doped graphene: Pyrolysis temperature regulation and catalyst regeneration mechanism, J. Hazard. Mater. 397 (2020), 122681.

[58] M. Yaldagard, N. Seghatoleslami, M. Jahanshahi, Preparation of Pt-Co nanoparticles by galvanostatic pulse electrochemical codeposition on in situ electrochemical reduced graphene nanoplates based carbon paper electrode for oxygen reduction reaction in proton exchange membrane fuel cell, Appl. Surf. Sci. 315 (2014) 222–234.

[59] Z.Z. Wang, P. Lv, Y. Hu, K.L. Hu, Thermal degradation study of intumescent flame retardants by TG and FTIR: Melamine phosphate and its mixture with pentaerythritol, J. Anal. Appl. Pyrol. 86 (2009) 207–214.

[60] G.B. Chernobay, Y.A. Chesalov, V.P. Baltakhinov, G.Y. Popova, T. V. Andrushkevich, In situ FTIR study of β-picoline transformations on V–Ti–O catalysts, Catal. Today 164 (2011) 58–61.

[61] A. Sionkowska, A. Planecka, Preparation and characterization of silk fibroin/chitosan composite sponges for tissue engineering, J. Mol. Liq. 178 (2013) 5–14.

[62] J.J. Li, R.J. Lu, B.J. Dou, C.Y. Ma, Q.H. Hu, Y. Liang, F. Wu, S.Z. Qiao, Z.P. Hao, Porous graphitized carbon for adsorptive removal of benzene and the electrothermal regeneration, Environ. Sci. Technol. 46 (2012) 12648–12654.

[63] S. Kukunuri, H. Noguchi, In situ spectroscopy study of oxygen reduction reaction intermediates at the Pt/acid interface: Surface-enhanced infrared absorbance spectroscopy, J. Phys. Chem. C 124 (2020) 7267–7273.

[64] Y. Li, W. Cheng, H. Su, X. Zhao, J. He, Q. Liu, Operando infrared spectroscopic insights into the dynamic evolution of liquid-solid (photo)electrochemical interfaces, Nano Energy 77 (2020), 105121.